ACS APPLIED MATERIALS & INTERFACES

www.acsami.org

Research Article

Stable Iron Oxide Nanoflowers with Exceptional Magnetic Heating Efficiency: Simple and Fast Polyol Synthesis

Liudmyla Storozhuk, Maximilian O. Besenhard, Stefanos Mourdikoudis, Alec P. LaGrow, Martin R. Lees, Le Duc Tung, Asterios Gavriilidis, and Nguyen Thi Kim Thanh*

Cite This: *ACS Appl. Mater. Interfaces* 2021, 13, 45870–45880

Read Online

ACCESS | Metrics & More | Article Recommendations | Supporting Information

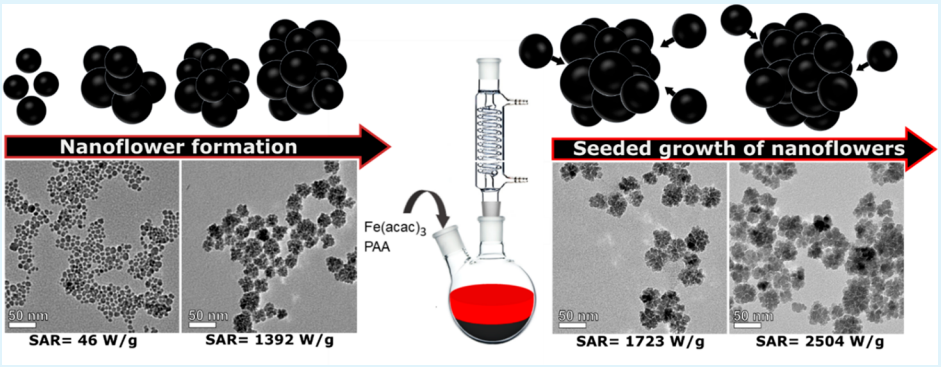

ABSTRACT: Magnetically induced hyperthermia has reached a milestone in medical nanoscience and in phase III clinical trials for cancer treatment. As it relies on the heat generated by magnetic nanoparticles (NPs) when exposed to an external alternating magnetic field, the heating ability of these NPs is of paramount importance, so is their synthesis. We present a simple and fast method to produce iron oxide nanostructures with excellent heating ability that are colloidally stable in water. A polyol process yielded biocompatible single core nanoparticles and nanoflowers. The effect of parameters such as the precursor concentration, polyol molecular weight as well as reaction time was studied, aiming to produce NPs with the highest possible heating rates. Polyacrylic acid facilitated the formation of excellent nanoheating agents iron oxide nanoflowers (IONFs) within 30 min. The progressive increase of the size of the NFs through applying a seeded growth approach resulted in outstanding enhancement of their heating efficiency with intrinsic loss parameter up to 8.49 nH m^2 kg_{Fe}^{-1}. The colloidal stability of the NFs was maintained when transferring to an aqueous solution via a simple ligand exchange protocol, replacing polyol ligands with biocompatible sodium tripolyphosphate to secure the IONPs long-term colloidal stabilization.

KEYWORDS: *polyol synthesis, iron oxide nanoparticles, nanoflower, seeded growth, ligand exchange, magnetic hyperthermia, intrinsic loss parameter (ILP)*

INTRODUCTION

The heat magnetic nanoparticles generate when exposed to an alternating magnetic field is the basis for many applications including catalysis,[1] antimicrobial materials,[2,3] and the most well-known and challenging magnetically induced hyperthermia (MIH) for cancer treatment.[4,5]

Due to the proven biocompatibility of iron oxide nanoparticles (IONPs), they are the most common magnetic nanoparticle system for biomedical applications having clinically been approved for example in magnetic resonance imaging and drug/nutrient delivery.[6,7] Although the first studies of MIH for cancer treatment date back to the 1950s,[8] it only got to the verge of becoming a standard treatment for certain cancer types in the past decade.[9,10] In fact, the use of superparamagnetic iron oxide NPs (SPIONs) as agents for MIH is becoming increasingly common. Another class of magnetic materials with promising MIH activity are magnetosomes. These composite structures are actually iron oxide NPs produced with the assistance of a strain of magnetotactic bacteria.[11,12]

As MIH for cancer treatment relies on the induced malignant cancer cell death after heating to temperatures above 40 °C, the IONPs' heating ability in an alternating magnetic field is the key to success. The better the particles heat, the lower is the required concentration of IONPs in the

Received: June 30, 2021
Published: September 20, 2021

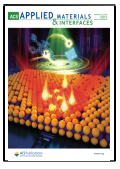

https://doi.org/10.1021/acsami.1c12323
ACS Appl. Mater. Interfaces 2021, 13, 45870–45880

tissue, hence, increasing the chance for efficient IONPs administration and reducing the risk of side effects.

A recent study of ours has shown that loading a chemotherapy drug, doxorubicin, onto magnetic nanoparticles that can heat up the cancer cells at the same time as delivering the drug to them was up to 34% more effective at destroying the cancer cells than the chemotherapy drug without added heat.[13]

The optimization of IONP properties for MIH is still a very active area of research. The heating ability is considered the critical factor and is usually prioritized when developing syntheses for MIH. As the heating abilities of IONPs depend not only on their intrinsic properties, but also on the frequency and strength of the applied magnetic field, the particle concentration and the medium in which they are dispersed, systematic comparison with literature can be challenging. However, there is strong evidence from early linear response theory models[14] and experimental studies[15,16] that monodisperse (single crystalline) IONPs above 10 nm and below 25 nm are the most promising candidates for MIH.

Recently, clustered nanostructures were shown to have superior heating characteristics than their building blocks, i.e., the smaller single crystals. This can in principle be explained as a result of the magnetic interactions between clustered particles.[17] These interparticle interactions are complex and depend strongly on the single crystal particle size, orientation and spacing. For example, when comparing particle clusters and single crystals of the same dimensions, the single particles display superior heating ability. However, an appealing feature of clustered structures is that they remain superparamagnetic (which is essential to avoid further agglomeration and hence precipitation) even when their dimension exceeds the superparamagnetic limit,[18] i.e., around 25 nm for IONPs.

Clustered IONPs have been synthesized by various methods, such as coprecipitation,[19−21] thermal decomposition,[22] microwave, hydrothermal/solvothermal, including sol−gel, and sono-chemical methods.[23,24] The polyol method, in which the polyol acts as solvent, reducing agent, and surfactant is an attractive method for preparing nanophase and micrometer sized particles with well-defined shapes and controlled particle sizes.[6,25] In comparison with the coprecipitation method, polyol routes for IONPs have several advantages. In particular, the relatively high reaction temperature of the polyol method favors IONPs with higher crystallinity and hence higher saturation magnetization.[26−28] In addition, the IONPs can be easily dispersed in aqueous media and other polar solvents because the surface of IONPs contains many hydrophilic ligands.

The influence of poly(acrylic acid) (PAA) concentration over the magnetic and structural properties of IONPs for the coprecipitation method has previously been reported.[29,30] Mi et al. showed that for the thermal decomposition of $Fe(acac)_3$ in polyol,[30] the increase of PAA concentration would contribute mostly at coating the particles, as the chance of a PAA molecule binding with multinanocrystal nuclei could be enhanced.

The nanoclusters synthesized with PAA are only soluble in nonpolar solvents due to the capped hydrophobic surfactant ligands, which limits their potential for biomedical applications, hence, it is necessary to render them water dispersible. Recent work with phosphonate anchored layers grafted on MNPs demonstrated that these moieties were proven to be better anchoring groups to the surface of NPs without perturbing their properties.[31,32] Sahoo et al. found that alkyl phosphonates and phosphates could be used for obtaining thermodynamically stable dispersions of magnetic ferrite NPs via formation of P−O−Fe bonding.[33] In another work, Majeed and coauthors reported the development of a new class of water-dispersible polyphosphate grafted Fe_3O_4 nanomagnets for cancer therapy.[34]

In addition to heating ability, colloidal stability, and biocompatibility, the reproducibility and scalability of a synthesis protocol are crucial for bringing IONPs closer to application.[35] As the latter are frequently neglected, the replication of MNPs with good heating abilities is difficult. Hence, there is still a need for robust well-established synthetic routes providing particles with a set of properties that lead to excellent heating ability.

In this work, we demonstrate the synthesis of iron oxide flower-like nanostructures with exceptional heating abilities in alternating magnetic fields. These nanoflowers exhibit superior intrinsic loss parameter (ILP) > 8.4 nH m^2 kg_{Fe}^{-1} that is ∼3 times higher than commercially available nanoheaters as well as magnetic nanostructures with similar composition and morphology reported in literature.[4]

Though our polyol-prepared IONP/NFs were readily dispersible in water after synthesis, their colloidal stability was improved after exchanging the (polyol) ligand with sodium tripolyphosphate using a straightforward one pot protocol. Finally, a novel seeded growth strategy is demonstrated leading to further increase of the IONF size and their corresponding heating ability. All studies were performed with the intention to provide simple synthetic procedures yielding high-quality particles for MIH that can be produced in a very short time.

RESULTS AND DISCUSSION

Effect of Reaction Time, Polyol, and Precursor Concentration on IONP Synthesis. Typical reaction times of 12 h or longer (such as overnight reactions)[6,36−38] is a challenge for large-scale production. Such long synthetic times are frequently used to obtain desired IONP crystallinity. Therefore, optimizing a synthesis in terms of scalability must target a trade-off between product quality and reaction time.

To achieve this compromise, the IONP synthesis was performed in triethylene glycol (TREG) with 0.13 M $Fe(acac)_3$ for reaction times of 30 min, 1 h, 6 h, and 24 h. The expected increase in IONP size with reaction time[6,39] was confirmed by transmission electron microscopy (TEM) analysis (Figure 1). For the shortest reaction time (30 min) relatively monodisperse particles of D_{TEM} = 7.5 ± 1.4 nm were obtained. Increasing the reaction time to 1 h, 6 h, or 24 h yielded D_{TEM} = 9.9 ± 1.7 nm, 10.9 ± 1.9 nm, or 12.4 ± 2.5 nm, respectively.

The X-ray diffraction (XRD) patterns (Figure S1, Supporting Information, SI) confirm that all reaction times resulted in IONPs of inverse spinel structure (i.e., the most magnetic form; magnetite (Fe_3O_4) or maghemite (γ-Fe_2O_3)). The crystallite size increased likewise with reaction time from D_{XRD} = 6.0 nm for 30 min to D_{XRD} = 9.2, 10.2, or 11.9 nm for 1 h, 6 h, or 24 h, respectively. The comparable diameters obtained from XRD and TEM indicate that IONPs were monocrystalline, which was also confirmed by high resolution TEM (HRTEM) (Figure S2, SI).

Although the IONP volume (= $D_{TEM}^3 \cdot \pi/6$) increased ∼5 fold from 30 min to 24 h (and ∼doubled after 1 h), the

https://doi.org/10.1021/acsami.1c12323
ACS Appl. Mater. Interfaces 2021, 13, 45870−45880

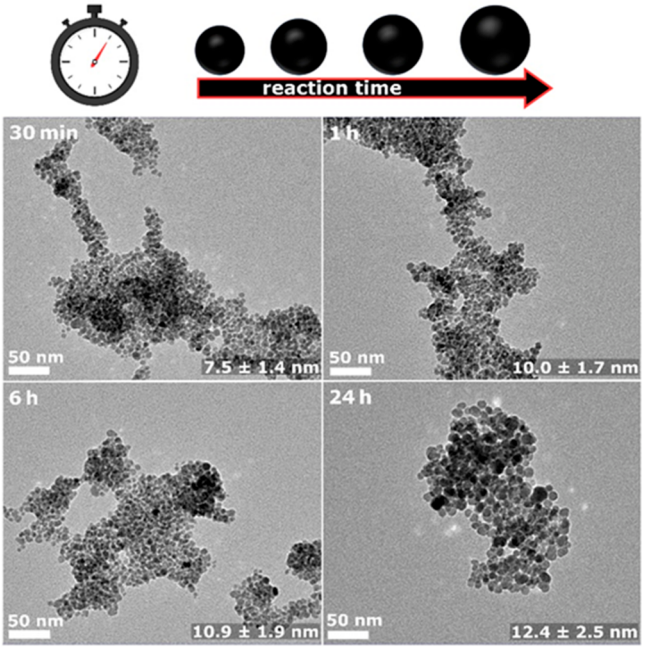

Figure 1. TEM images of IONPs synthesized in TREG with 0.13 M $Fe(acac)_3$ and reaction times of 30 min, 1 h, 6 h, and 24 h.

concentration of Fe in IONPs ($C_{Fe\text{-}IONP}$) did not increase by more than 20% (comparing with syntheses performed for 30 min and 24 h, see Table S1, SI). This indicates that for longer reaction times the IONPs grew by coalescence and/or Ostwald ripening.[40] The latter, however, is unlikely as the required dissolution of small particles cannot be justified by the low (not quantified) solubility of magnetite/maghemite IONPs in polyols. It should be noted that polyol methods are in general associated with low precursor conversions, i.e., the $C_{Fe\text{-}IONP}$ is expected to be significantly lower than the total Fe concentration − $C_{Fe\text{-}total}$ (in particles and solution).[27]

As expected, the IONP heating ability increased with the synthetic time (i.e., with the IONP size) from negligible heating performance for 30 min (SAR = 64 W g_{Fe}^{-1}) to an SAR of 219 W g_{Fe}^{-1} for the 24 h synthesis (Figure S3 and Table S1, SI). The suggested growth mechanisms imply that for longer reaction times a further increase in IONP size ≫10 nm, may be possible and this could lead to higher heating efficiency;[15,16] however, such long reaction times are not practical from the scalability point of view. When fixing the reaction time to 30 min, it was possible to further increase the IONP size to D_{TEM} = 8.2 ± 1.5 nm (Figure S4, SI) by changing TREG with tetraethylene glycol (TEG), which was shown to yield larger IONPs.[41] However, both syntheses yielded small (<10 nm) IONPs with poor heating ability (Figure S3 and Table S1, SI), indicating that for such short reaction times the synthesis of IONP clusters is a better option to produce particles with sufficient heating efficiency for MIH. XRD analysis (Figure 2) of IONPs synthesized using different iron precursor concentrations, i.e., 0.07 and 0.13 M $Fe(acac)_3$ and different polyols (TREG and TEG) showed that all peaks can be indexed to the cubic inverse spinel structure (e.g., of magnetite Fe_3O_4) and that no crystalline impurities could be found. Evaluation of the crystallite size using the Scherrer equation yielded D_{XRD} = 5.1 nm and D_{XRD} = 8.1 nm for IONPs synthesized using TREG and TEG (both at 0.07 M $Fe(acac)_3$) respectively. IONPs synthesized with 0.13 M $Fe(acac)_3$ in

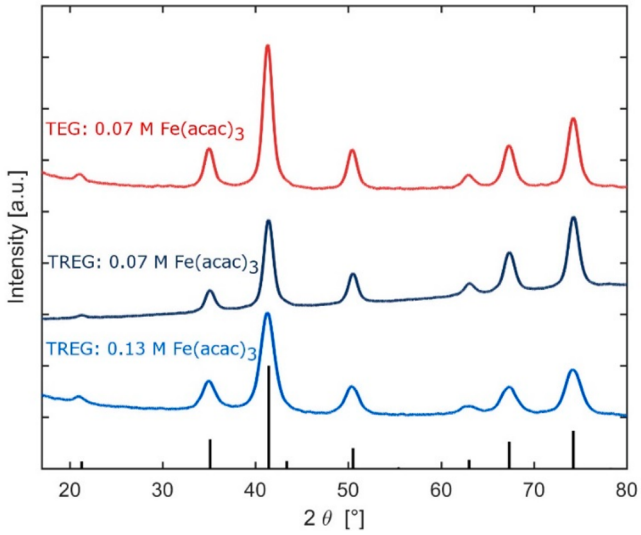

Figure 2. XRD patterns of IONPs synthesized in TREG at different iron precursor concentrations and in TEG with reaction times of 30 min. The bars at the bottom show the peak positions and relative intensities corresponding to magnetite (JCPDS card 03−065−3107).

TREG had D_{XRD} = 6 nm. The results are consistent with TEM, showing that the increasing of polyol chain length and of iron precursor concentration leads to an increase of the size of the obtained IONPs.

IONF Synthesis Using PAA. To achieve IONP clustering within 30 min of reaction time, the synthesis was performed in the presence of PAA (20−100 mM).

Figure 3 shows the FTIR spectrum of dried iron oxide nanoflowers (IONFs) synthesized with 66 mM PAA, together with the corresponding spectrum of dried PAA alone. The

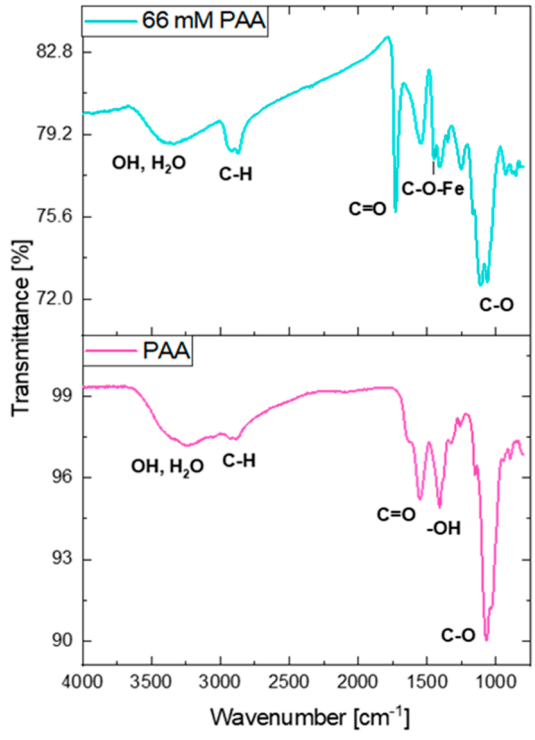

Figure 3. Fourier transform infrared spectra of IONFs (top) and PAA (bottom).

https://doi.org/10.1021/acsami.1c12323
ACS Appl. Mater. Interfaces 2021, 13, 45870−45880

spectrum of IONFs (Figure 3 top) shows several absorptions in the investigated 4000−600 cm^{-1} range, corresponding to the vibrational modes of PAA. In particular, the bands are assigned to the asymmetric and symmetric CH_2 stretching (2922, 2860, and 2917, 2868 cm^{-1}, for free PAA and PAA-capped IONP respectively), to the C═O bond stretching (1728−1554 cm^{-1}), to O−H stretching mode of carboxylate groups (1400−1408 cm^{-1}) and to CH deformation (1463 and 1377 cm^{-1}). The peak at 1450 cm^{-1} could be attributed to the asymmetric C−O−Fe stretching mode of carboxylate groups covalently bonded with ferric or ferrous ions on the surface of the particles, which indicated that PAA coating was achieved by carboxylic groups coordinating with iron atoms.[42]

TEM analysis (Figure 4a) showed that IONPs were clustered successfully, and that cluster size and structure could be tuned via the adjustment of PAA concentration. While single core particles were obtained without PAA (0.07 M $Fe(acac)_3$, TREG) with D_{TEM} = 6.1 ± 2.1 nm (Figure S4, SI), IONP aggregation occurred at 20 mM PAA (otherwise in identical synthetic conditions) yielding polydisperse IONP clusters, D_{TEM} = 9.8 ± 3.6 nm. When increasing the amount of PAA to 33, 66, and 100 mM well-defined and monodisperse "nanoflowers" were obtained with D_{TEM} = 20.5 ± 2.4, 22.7 ± 2.1, and 26.2 ± 1.7 nm, respectively.

Thus, TEM and XRD analyses (Figure S5, SI) show that while an increase in PAA concentration resulted in larger IONP clusters, the crystallite size remained constant (Table S1, SI). This confirms the multicore nature of IONPs synthesized with PAA, which is consistent with previous reports. For example, Hemery et al. reported ∼7.4 nm grain sizes for polyol-prepared multicore maghemite NFs with an outer diameter of about 36.9 nm.[43] Palchoudhury et al. prepared IONFs, using 1-octadecene as solvent with oleic acid, trioctylphosphine-oxide, and iron oleate as precursor. They report that IONF formation requires a high nuclei concentration which, after a growth stage consuming the monomers, aggregate to minimize the surface energy, forming IONFs.[44] It has to be noted that IONFs prepared by polyol method can still be single-crystalline, constituted of small grains with the same crystalline orientation, despite being classified as "multicore".[45] Still, higher specific heating rates of multicore IONPs compared to single core ones have been attributed to "spin glass" dynamics of the magnetic moments within a cluster, strongly correlated with the exchange interaction.[46] In fact, it has been shown that multicore particles can display enhanced susceptibility compared to single core, while maintaining a superparamagnetic behavior due to a reduced surface anisotropy.[47]

The heating ability of the single core IONPs and clustered IONPs (i.e., IONFs) in an alternating magnetic field shows a clear enhancement of the SAR for IONFs (Table 1, Figure 4b). The SAR was enhanced with increasing PAA concentrations reaching 915 W g_{Fe}^{-1} (ILP = 3.0 nH m^2 kg_{Fe}^{-1}) for IONFs synthesized with 66 mM PAA. The increase in heating efficiency is attributed to the structural and magnetic properties of the IONFs, which are composed of highly ordered nanocrystals that do not behave like isolated grains.[48,49] It is worth noting that it is crucial for efficient magnetic hyperthermia, when the crystal domains rearrange forming from single crystalline structures.[50]

From the above, one can observe the nonlinear modification of SAR and ILP values with the increase of NP size. However, repeated measurements confirmed the reproducibility and

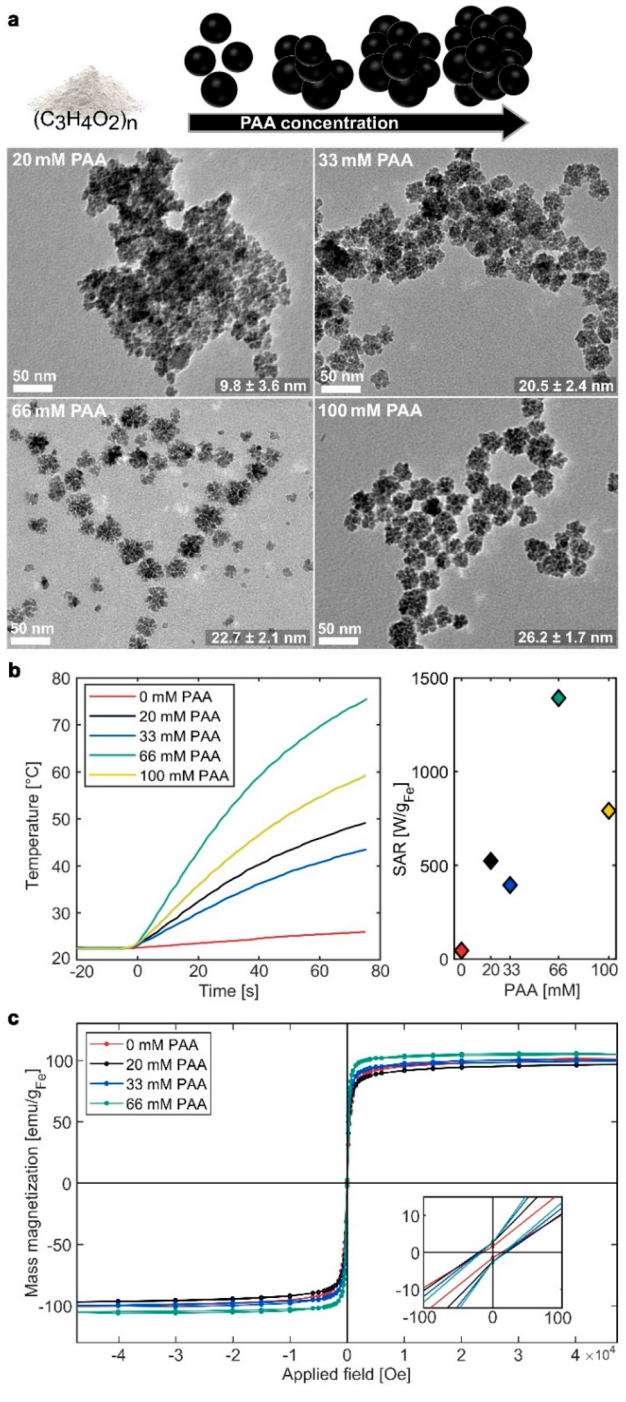

Figure 4. TEM images of clustered IONFs synthesized in TREG with 0.07 M $Fe(acac)_3$ and reaction time of 30 min using 20, 33, 66, and 100 mM PAA (a). Heating profiles of IONFs solutions (left) and the SAR values (right) (b). Hysteresis curves of IONFs synthesized with different concentrations of poly(acrylic acid) measured at 300 K. The insets show the magnified hysteresis loop at low fields (c).

validity of such big increase for the SAR for only few nanometers of size difference. We would like to highlight that it is not expected to necessarily observe a linear correlation between the heating efficiency and the IONP size.[51] Even if 2 nm (i.e., 20.5 nm for NFs with 33 mM PAA and 22.7 nm for NFs with 66 mM PAA) is a small difference in size, the actual arrangement of the crystal domains within the NFs may be somewhat different between the two samples, and the magnetic

https://doi.org/10.1021/acsami.1c12323
ACS Appl. Mater. Interfaces 2021, 13, 45870−45880

Table 1. Characterization Summary of Single Core IONPs (0 mM PAA) and IONFs (20-100 mM PAA) with Total Fe Concentration ($C_{Fe\text{-}total}$ = 3.66 mg_{Fe} mL^{-1}), Fe Concentration Obtained by ICP ($C_{Fe\text{-}IONP}/C_{Fe\text{-}IONF}$), Particle Diameter Obtained by TEM (D_{TEM}), Crystallite Diameter Obtained by XRD (D_{XRD}), as Well as Heating Characteristics

PAA (mM)	D_{XRD} (nm)	D_{TEM} (nm)	$C_{Fe\text{-}IONP}/C_{Fe\text{-}IONF}$ (mg_{Fe} mL^{-1})	slope (°C s^{-1})	SAR (W g_{Fe}^{-1})	ILP (nH m^2 kg_{Fe}^{-1})
0	5.2	6.1 ± 1.2	2.65	0.048	46	0.15
20	9.3	9.8 ± 3.6	2.24	0.47	524	1.78
33	11.2	20.5 ± 2.4	2.16	0.34	395	1.34
66	**11.0**	22.7 ± 2.1	**1.78**	**0.99**	**915**	**3.0**
100	10.8	26.2 ± 4.7	1.99	0.63	442	1.46

coupling could be also different in a considerable extent. This might cause a much improved heating efficiency for the bigger size sample. The different amount of PAA also seems to affect significantly the heating efficiency behavior and to be more important than particle size, possibly because the actual arrangement of the crystal domains within the NFs and the magnetic coupling are different at distinct PAA concentrations.

When increasing the PAA concentration to 100 mM the SAR dropped (despite an increase in NF size) to 442 W g_{Fe}^{-1} (ILP = 1.46 nH m^2 kg_{Fe}^{-1}) indicating that higher PAA concentration deteriorates the magnetic coupling. The solution became highly viscous at room temperature which hampered the ligand exchange step, hence, 100 mM PAA samples were not considered for further investigation.

Magnetic hysteresis curves measured at 300 K (Figures 4c and S6 measured at 5 K, SI) show that the single core IONPs (0 mM PAA) and IONFs (20, 33, and 66 mM PAA) were superparamagnetic. Their coercivities were lower than 50 Oe (13.5, 20, 18.3, and 17 Oe) and mass magnetization values were 100.8, 96.9, 100, and 105 emu g_{Fe}^{-1} respectively. This is in line with the zero-field cooled and field cooled curves (Figure S7, SI), showing higher blocking temperatures (T_B) for larger IONFs. Isolated single core IONPs showed a $T_B \sim 160$ K, whereas IONFs had T_B of ~209, 283, and 302 K, for 20, 33, and 66 mM PAA respectively. Since IONFs obtained at 66 mM PAA exhibited a T_B around room temperature, they are borderline superparamagnetic. The broad peak of the zero-field cooled curve around T_B for all NFs samples indicate stronger magnetic interactions, as expected for such large multicore IONPs.[52,53] The mass magnetization was normalized to the weight of the magnetic portion of the particles; thermogravimetric analysis (TGA) measurements (Figure S8, SI) helped to determine the organic mass amount, which is not magnetic.

Ligand Exchange and Stability Study. The surface modification of IONFs by sodium tripolyphosphate (STPP) was performed as described in the Methods section. FTIR results (Figure S9, SI) demonstrate that STTP successfully substituted the TREG molecules adsorbed on IONPs during the ligand exchange step. After the STTP ligand exchange, the characteristic bonds of PAA disappeared, while P−O and P═O stretching bands from STPP appeared, located between 1200 and 1300 cm^{-1}.[54]

Replacing polyol ligands with STPP increased the electrostatic and steric repulsion significantly, which ensured the IONFs long-term colloidal stabilization. The hydrodynamic diameter of STPP-capped IONPs was D_h = 78 nm and did not show any further increase after more than three months (Figure S10, SI).

The size of IONFs did not change after dialysis (D_{TEM} = 32 ± 5.3 nm (Figure S11, SI)). XRD analysis (Figure S12, SI) shows that the ligand exchange reaction had no effect on the crystal structure and crystallite size, which remained at D_{XRD} = 10 nm.

IONF Size Increase via Seeded Growth. A seeded growth strategy was used (see section Methods) to further increase the IONFs size, aiming to improve their heating ability. Seeded growth was performed using the IONF synthesis with 66 mM PAA, as these IONFs displayed the best heating ability (see Table 1).

TEM analysis (Figure 5a) showed an increase in IONF size with each feeding step, i.e., fromD_{TEM} = 22.5 ± 2.9 nm (IONF seeds) to D_{TEM} = 29.7 ± 4.1 nm after the first feeding step, and after the second feeding step to D_{TEM} = 32.5 ± 6.1 nm. XRD

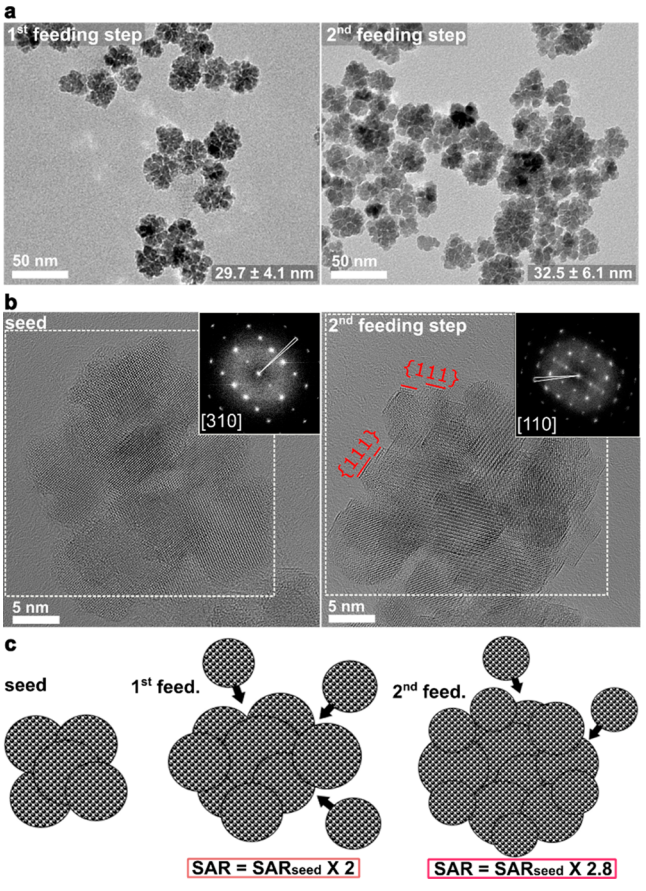

Figure 5. TEM images of the IONFs synthesized with PAA via seeded growth: 1st and 2nd feeding step (a). Aberration corrected transmission electron micrograph of IONF seeds and after the 2nd feeding step. The red lines show the low index {111} facets. The insets show the FFT taken from the dashed white box, with the iron oxide viewed down the [310] zone axis in a, and [110] zone axis in b. The white lines in the FFT show the angle of variation in the FFT spot (b). Schematic representation of seeded growth mechanism (c).

https://doi.org/10.1021/acsami.1c12323
ACS Appl. Mater. Interfaces 2021, 13, 45870−45880

Table 2. Characterization Summary of PAA-IONFs Seeds and After 1 or 2 Feeding Steps of Seeded Growth with Total Fe Concentration ($C_{Fe\text{-}total}$ = 3.66 mgFe mL^{-1}), Fe Concentration Obtained by ICP ($C_{Fe\text{-}IONF}$), Particle Diameter Obtained by TEM (D_{TEM}), Crystallite Diameter Obtained by XRD (D_{XRD}), as Well as Heating Characteristics

	D_{XRD} (nm)	D_{TEM} (nm)	$C_{Fe\text{-}IONF}$ (mg_{Fe} mL^{-1})	slope (°C s^{-1})	SAR (W g_{Fe}^{-1})	ILP (nH m^2 kg_{Fe}^{-1})
seeds	10.7	22.5 ± 2.9	1.23	0.42	855	2.9
1st feeding step	10.6	29.7 ± 4.1	0.93	0.64	1723	5.8
2nd feeding step (repeated 3 times)	13.1 ± 0.3	31.8 ± 5.1	1.13 ± 0.17	1.06 ± 0.24	2426 ± 76	8.08 ± 0.41

(Figure S13, SI) revealed that the core size changed only slightly from D_{XRD} = 10.7 nm (IONF seeds) to D_{XRD} = 10.6 nm after the first feeding step, and after the second feeding step to D_{XRD} = 13.4 nm.

HRTEM comparison of IONFs before (= seeds) and after the second feeding step revealed that both are made up of aligned grains viewed down a single zone axis (Figure 5b). For the IONF seed, the particle was viewed down the [310] zone axis. The broadening of the spot in the Fourier transformed images (Figure 5b insert) indicates a slight lattice mismatch between the single cores and reflects a deviation in the grain orientation (arcing in the spots is shown by the white lines in the inset) of 2.2 ± 0.6°. The grown IONF is seen to be highly faceted with predominantly {111} facets exposed on its surface. The IONF is viewed down a single [110] zone axis, with a deviation in the grain orientation (white lines in the inset) being 2.1° (seeds) and 3.4° (after the 2st feeding step). This shows that the IONFs are made up of aligned crystalline domains deviating by only a small angle, which increased as the IONFs grew larger.

The HRTEM, TEM and XRD indicate that seeded IONF growth took place by coalescence, as sketched in Figure 5c. During each feeding step, growth occurred by aligned aggregation of newly formed single core crystals and more of these single core building blocks were added with each feeding step.

The absence of significant increase of the core size, as well as the slightly misaligned grains is in line with the magnetic measurements confirming that the IONPs remain superparamagnetic even after the second feed addition (Figure S14, SI).

Magnetic hyperthermia requires particles with relatively high saturation magnetization, high magnetic susceptibility and a zero or very low coercivity.[55] The magnetic measurements (Figure S7, SI) confirm that the IONFs remain superparamagnetic even after the second feed addition. One reason to prefer (nearly) superparamagnetic NPs over ferro/ferrimagnetic NPs is that the absence of coercive forces minimizes the intensity of magnetic dipolar interactions and, therefore, reduces the likelihood of NP aggregation that could have harmful effects on the body circulatory system.

The heating ability increased significantly with each feeding step, doubling after the first (SAR = 1723 W g_{Fe}^{-1}), and almost tripling after the second feeding step to SAR = 2426 W g_{Fe}^{-1}, i.e., an ILP = 8.08 ± 0.41 nH m^2 kg_{Fe}^{-1} (see Table 2, Figure S15 for heating profiles, Figure S16 for overall trend, SI). It is possible that the particularly high heating efficiency of the IONFs of the current work is attributed at least to some extent to defects in their crystal structure. The cores which compose the NFs are not perfectly aligned and the amount of misalignment increases in the seeded particles. This might imply the presence of defects in the IONFs. Lappas et al. have shown that defects such as vacancies endow better hyperthermia performance over defect-free nanocrystals.[56] Also, the seeded grown, still superparamagnetic, nanoflowers exceeded the size of previously reported IONFs. Therefore, enhanced magnetic coupling in these superparamagnetic nanoflowers is expected to have a positive impact on the heating rate.

The heating rate, best compared using the ILP, of the seeded grown IONF is more than twice as high as those of commercially available IONPs for magnetic hyperthermia (ILP < 4 nH m^2 kg_{Fe}^{-1}),[57,58] and clearly surpasses other IONPs, such as single crystalline IONPs, e.g., cubes (SAR ∼ 300−400 W g_{Fe}^{-1}, ILP = 0.36−0.47 nH m^2 kg_{Fe}^{-1}),[59−61] and other IONFs synthesized previously. For example, for 22 nm magnetite IONFs prepared by polyol route,[36] SAR up to 1180 W g_{Fe}^{-1} was measured with ILP values up to 2.6 nH m^2 kg_{Fe}^{-1}. Hugounenq et al.[48] reported SAR values up to 1992 W·g^{-1} (ILP = 6.1 nH m^2 kg_{Fe}^{-1}) for 24 nm IONFs prepared using diethylene glycol.

In addition, the synthesis was proven to be reproducible with IONF exhibiting excellent heating rates repeatedly (see Table S1, SI). This is important to highlight, since successful reproducibility cannot always be taken for granted upon the use of colloidal chemical routes for NP synthesis. The PAA-induced aggregation mechanism seems to yield IONFs not only faster (within 30 min, which is significantly faster than with previous syntheses), but also in a more controllable way, this concerns the initial IONF formation but also their subsequent seeded growth stage.

Some reports claimed that the allowable values of H × f are much larger than the Atkinson-Brezovich limit,[62] ranging between 1.8 × 10^9 A $m^{-1}s^{-1}$;[63] to 8.3 × 10^9 A $m^{-1}s^{-1}$[64] and up to 18.7 × 10^9 A $m^{-1}s^{-1}$.[65] It should be mentioned that a high frequency (765 kHz) has also been employed in in vitro studies to achieve a decent level of heating efficiency.[66]

However, for the sake of accuracy in determining the particles heating rates, (e.g., using the initial slope method)[67] as shown here (and also elsewhere) large heating rates are preferred. This aims to minimize the effect of cooling due to heat transfer, i.e., to justify the assumption of (pseudo) adiabatic heating. In fact, such high frequencies, as the ones used herein are commonly applied to quantify heating rates.

The somewhat lower values obtained at lower frequencies can be explained by the heat losses that need to be considered for slow heating during such calorimetric measurements (Figure S17, SI).

CONCLUSIONS

In summary, we present a simple, fast, and reproducible (hence scalable) one-pot synthesis and ligand exchange of IONPs yielding IONFs with excellent heating ability (ILP = 8.08 ± 0.41 nH m^2 kg_{Fe}^{-1}). The synthesis was green and cost-effective avoiding expensive or toxic chemicals. Via a simple ligand exchange protocol the synthesized IONPs and IONFs became highly colloidally stable in water with no change in the hydrodynamic diameter for more than three months.

https://doi.org/10.1021/acsami.1c12323
ACS Appl. Mater. Interfaces 2021, 13, 45870−45880

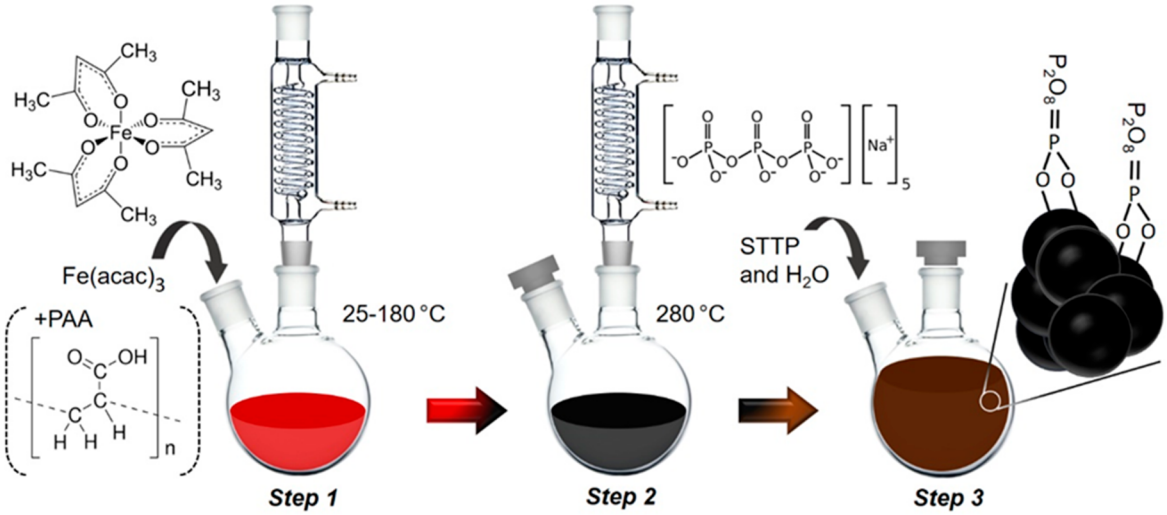

Figure 6. Schematic of simple one-pot thermal decomposition of $Fe(acac)_3$ polyol synthesis yielding single core IONPs (without poly(acrylic acid)) and IONFs (with poly(acrylic acid)) in Step 1 and Step 2, that are highly stable in water after exchanging the polyol ligand with sodium tripolyphosphate in Step 3.

The IONP synthesis in polyol was systematically studied in terms of the effect of precursor concentration, the polyol used, and the reaction time on the particles size and heating properties. The lowest possible reaction time (30 min) was chosen assuring that developed syntheses are scalable. Syntheses yielding single core particles were only able to result in a low heating ability (SAR = 219 W g_{Fe}^{-1}, ILP = 0.63 nH m^2 kg_{Fe}^{-1}) for reaction times of 24 h.

IONFs synthesized within 30 min in the presence of PAA exhibited remarkably improved heating rates. By tuning the concentration of PAA, IONP clustering was controlled, producing (at 66 mM PAA) monodisperse IONFs (D_{TEM} = 22.7 ± 2.1 nm) with heating rates of SAR = 915 W g_{Fe}^{-1} (ILP = 3.0 nH m^2 kg_{Fe}^{-1}).

A seeded growth approach was demonstrated for the first time to increase the size of the IONFs size further. HRTEM, XRD and magnetometry illustrated that initially formed IONFs and seeded grown IONFs consist of single crystalline building blocks that aggregate fairly aligned, but with a slight misalignment. The seeded grown nanoflowers, hence, remained superparamagnetic, but their heating properties improved. After only one feeding step (D_{TEM} = 29.7 ± 4.1 nm) the heating rate doubled and almost tripled after a second feeding step (SAR = 2426 ± 76 W g_{Fe}^{-1}, i.e., ILP = 8.08 ± 0.41 nH m^2 kg_{Fe}^{-1}).

Considering the excellent heating rates of these IONFs synthesized within a short reaction time (30 min at 280 °C for seed generation and per feeding step), and their excellent colloidal stability after a simple ligand exchange step (feasible as the synthesis is performed in polyols) these materials are promising candidates for use as heating agents in cancer treatment. The presented synthetic pathway provides a facile benchmark synthesis to reproducibly synthesize colloidally stable and biocompatible magnetic nanoparticles (MNPs) with excellent heating abilities for magnetically induced hyperthermia cancer treatment.

METHODS

Chemicals. Iron(III) acetylacetonate ($Fe(acac)_3$, 99.9%; Merck Millipore), triethylene glycol (TREG, 99%; Sigma-Aldrich), tetraethylene glycol (TEG, 99%; Sigma-Aldrich), ethyl acetate (EtAc, 99.8%; Sigma-Aldrich), sodium tripolyphosphate (STTP, Alfa Aesar), and poly(acrylic acid) (PAA, M_w = 1800 Da; Sigma-Aldrich), nitric acid (70% HNO_3 for inductively coupled plasma mass spectrometry (ICP), 99.999% trace metal basis; Sigma-Aldrich), Fe standard for ICP (TraceCERT, Sigma-Aldrich) were used as received without any further purification.

IONP Syntheses. IONPs were produced via a modified thermal decomposition synthesis in polyols.[41,68] For a typical synthesis, the precursor solution was prepared by dissolving $Fe(acac)_3$ in the polyol (either TREG and TEG), yielding a 0.07 or 0.13 M $Fe(acac)_3$ final solution (depending on the initial concentration used). The precursor solution was heated from room temperature to 180 °C at 3 °C/min and kept at this temperature, i.e., just before thermally decomposing $Fe(acac)_3$. Next, the temperature was increased to 280 °C at 5 °C/min, and the reaction mixture was held at this temperature for reaction times set between 30 min and 24 h before cooling to room temperature. The solution was magnetically stirred (500 rpm) throughout the synthesis.

Following the work of Mi et al.[30] showing that the addition of PAA can yield clustered IONPs, the synthesis was also performed in the presence of PAA in a range of different concentrations (0.02−0.1 M). The experimental procedure (with PAA) is shown in step 1 and 2 in Figure 6. Table S1, SI, shows a summary of all IONP synthesis performed.

IONF Ligand Exchange. The IONFs were stable in the polyol solution in which they were synthesized, but not in aqueous solutions. After washing and redispersion in deionized water (keeping the IONF concentration constant), sedimentation became evident after ∼1 d (which is typical for IONFs stabilized by polyols only). To achieve long-term colloidal stability in water, the polyol ligand had to be exchanged. Following the facile ligand exchange protocol by Wan et al., surface polyol ligands were exchanged with STPP, i.e., a biocompatible stabilizer.[69]

To secure the attachment of STTP on the IONFs surface, aqueous STTP solution (200 mL of a 2.5 mM) was added under vigorous stirring to IONF polyol solution (30 mL) (see Figure 6, step 3). The resulting IONF solution (13%$_{vol}$ polyol, 87%$_{vol}$ water) was kept overnight under moderate stirring to ensure successful ligand exchange of the polyol (TREG) with STTP. To remove excess STTP, unreacted precursor, and the polyol, the STPP-capped IONFs were purified by dialysis against deionized water in a cellulose acetate dialysis bag (Spectra/Por 12 000−14 000 g mol^{-1} molecular weight cutoff (MWCO), Standard RC Trial Kit) for 72 h at room temperature, during which the water was replaced frequently.

https://doi.org/10.1021/acsami.1c12323
ACS Appl. Mater. Interfaces 2021, 13, 45870−45880

Seeded Growth of IONFs. A seeded-growth approach was carried out to further increase the size of IONFs which were formed in the presence of PAA. More specifically, a selected volume of precursor solution (typically 10 mL) was added at room temperature to a previously synthesized IONF solution. The latter was synthesized from an identical precursor solution; hence, the Fe molarity remained constant in all precursor solutions, before and during the seeded growth. After adding the precursor, the mixture was magnetically stirred for 5 min and then heated as described in the section IONP Syntheses. The procedure of one feeding step is sketched in Figure 7. After each feeding step the IONP solutions were cooled to room temperature to terminate the growth.

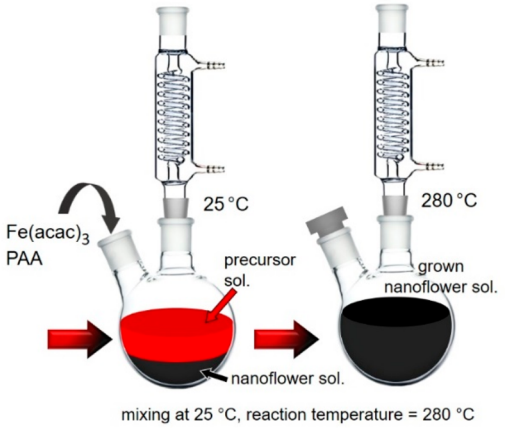

Figure 7. Schematic depicting of one feeding step for seeded growth of IONP NFs.

IONP Characterization. IONPs not designated for ligand exchange were precipitated with ethyl acetate (2:1 vol_{EtAc}: vol_{sample}), magnetically decanted and washed with excess ethanol in triplicate before analysis.

TEM images were captured using a JEOL 1200 EX microscope at a 120 kV acceleration voltage. IONP suspensions (after redispersion in deionized water) were drop-casted on carbon-coated copper grids and air-dried at room temperature. Particle size analysis from TEM images was performed manually using the image analysis software ImageJ. For nonspherical particles, the particle size was obtained by taking the average value between the maximum diameter and the diameter at a 90° angle to the maximum diameter. For each sample >200 particles were measured to determine the average diameter and standard deviation ($D_{TEM} \pm \sigma_{TEM}$). Aberration corrected HRTEM was performed in a Titan Themis 60−300 equipped with an image corrector, probe corrector, and monochromator at 200 kV.

X-ray diffraction (XRD) patterns of dried samples were obtained using a PANalytical X'Pert3 (Malvern Panalytical) diffractometer equipped with a CoKα radiation source (λ = 1.79 Å) operated at 40 mA. The crystallite diameter (D_{XRD}) was evaluated from full width half-maximum (fwhm) intensity of the most intense diffraction peak, i.e., of the {311} planes, diffracted at 2θ = 41° using the Scherrer equation:

$$D_{XRD} = 0.89 \times \frac{\lambda}{FWHM} \times \cos(\theta)$$

Fourier transformation infrared (FTIR) spectra were recorded using an attenuated total reflectance probe (Spectrum 100 FTIR, PerkinElmer).

Dynamic light scattering (DLS) was performed for ligand exchanged IONPs with a Zeta-Sizer Nano-ZS (ZEN 3600, Malvern Instruments, Ltd) at 22 °C. IONP solutions were diluted with deionized water until the hydrodynamic diameter (D_h) obtained plateaued (typically after a 4-fold dilution).

The concentration of Fe in the IONPs or IONFs ($C_{Fe\text{-}IONP}$, $C_{Fe\text{-}IONF}$) was identified by Inductively Coupled Plasma analysis, multicollector, mass spectrometry (ICP-MC-MS). First, the samples were washed (as described above) and weighed before dissolution in concentrated nitric acid at 60 °C. Thereafter, these solutions were diluted with deionized water to obtain a 2% nitric acid solution (the same as the standards used for calibration) for Fe quantification using a Varian 720 ICP-AES (Agilent).

The IONP magnetic properties were characterized by acquiring M−H plots with applied fields up to 50 kOe and zero-field-cooled (ZFC) and field-cooled (FC) magnetization versus temperature measurements (from 300 to 5 K) in 100 Oe, obtained with an MPMS superconducting quantum interference device (SQUID) magnetometer (MPMS-5S SQUID Magnetometer, Quantum design).

TGA was performed with a Discovery TGA (TA Instruments) under a nitrogen gas atmosphere between room temperature up to over 500 °C with a heating rate of 10 °C min^{-1}.

The particles heating abilities in an alternating magnetic field were evaluated with a calorimetric analyzer (G2 driver D5 series, nB nanoScale Biomagnetics) at frequency (f) of 488 kHz and a field strength (H) of 308 Oe (= 25 kA m^{-1}). The temperature was recorded with a GaAs-based fiber optic probe immersed in a vial containing ~1 mL of the IONP solution. A sealed glass (Dewar flask at <0.1 Pa) provided thermal insulation of the sample vial, rendering it a pseudoadiabatic system. The particles specific absorption rate (SAR), i.e., the power dissipated by the magnetic particles, was obtained by

$$SAR = c_{sol} \times \frac{\Delta T}{\Delta t} \times \frac{m_{sol}}{m_{IONP}}$$

Here c_{sol} is the specific heat capacity of the IONP solution (approximated by the solvent specific heat capacity), and m_{sol}/m_{IONP} is the sample solution to IONP mass ratio. $\Delta T/\Delta t$ was determined using the initial slope method via a linear fit through the first 20 s of the heating profile $T(t)$ after applying the alternating magnetic field. Since the heating efficiency of a given material depends on the field strength and frequency used, the ILP was determined to allow a better comparison with the literature.[70]

$$ILP = \frac{SAR[W/kg]}{f[kHz] \times H^2[(kA/m)^2]}$$

■ ASSOCIATED CONTENT

Supporting Information

The Supporting Information is available free of charge at https://pubs.acs.org/doi/10.1021/acsami.1c12323.

Additional experimental details, TEM-HRTEM images, XRD, TGA, FTIR, and SQUID measurements as well as further heating efficiency experiments (PDF)

■ AUTHOR INFORMATION

Corresponding Author

Nguyen Thi Kim Thanh − *Biophysics Group, Department of Physics and Astronomy, University College London, London WC1E 6BT, United Kingdom; UCL Healthcare Biomagnetics and Nanomaterials Laboratories, London W1S 4BS, United Kingdom;* orcid.org/0000-0002-4131-5952; Email: ntk.thanh@ucl.ac.uk

Authors

Liudmyla Storozhuk − *Biophysics Group, Department of Physics and Astronomy, University College London, London WC1E 6BT, United Kingdom; UCL Healthcare Biomagnetics and Nanomaterials Laboratories, London W1S 4BS, United Kingdom*

Maximilian O. Besenhard − *Department of Chemical Engineering, University College London, London WC1E 7JE, United Kingdom;* orcid.org/0000-0002-5079-617X

https://doi.org/10.1021/acsami.1c12323
ACS Appl. Mater. Interfaces 2021, 13, 45870−45880

Stefanos Mourdikoudis − *Biophysics Group, Department of Physics and Astronomy, University College London, London WC1E 6BT, United Kingdom; UCL Healthcare Biomagnetics and Nanomaterials Laboratories, London W1S 4BS, United Kingdom*

Alec P. LaGrow − *International Iberian Nanotechnology Laboratory, Braga 4715-330, Portugal;* orcid.org/0000-0002-3306-6458

Martin R. Lees − *Superconductivity and Magnetism Group, Physics Department, University of Warwick, Coventry CV4 7AL, United Kingdom*

Le Duc Tung − *Biophysics Group, Department of Physics and Astronomy, University College London, London WC1E 6BT, United Kingdom; UCL Healthcare Biomagnetics and Nanomaterials Laboratories, London W1S 4BS, United Kingdom*

Asterios Gavriilidis − *Department of Chemical Engineering, University College London, London WC1E 7JE, United Kingdom;* orcid.org/0000-0003-3508-5043

Complete contact information is available at: https://pubs.acs.org/10.1021/acsami.1c12323

Author Contributions

The manuscript was written through contributions of all authors. All authors have given approval to the final version.

Funding

The research was supported by EPSRC UK (EP/M015157/1).

Notes

The authors declare no competing financial interest.

■ ACKNOWLEDGMENTS

The authors would like to thank EPSRC U.K. for financial support (EP/M015157/1) through the Manufacturing Advanced Functional Materials (MAFuMa) scheme and UCL's EPSRC Impact Acceleration Account. N.T.K.T. and L.D.T. acknowledge the support from AOARD (FA2386-17-1-4042 Award). This work was carried out in part through the use of the INL Advanced Electron Microscopy, Imaging and Spectroscopy Facility. Authors thank Sayan Pal for supplementary heating efficiency measurements.

■ REFERENCES

(1) Asensio, J. M.; Miguel, A. B.; Fazzini, P.; van Leeuwen, P. W. N. M.; Chaudret, B. Hydrodeoxygenation Using Magnetic Induction: High-Temperature Heterogeneous Catalysis in Solution. *Angew. Chem., Int. Ed.* **2019**, *58* (33), 11306−11310.

(2) Nguyen, H.; Ohannesian, N.; Bandara, P. C.; Ansari, A.; Deleo, C. T.; Rodrigues, D.; Martirosyan, K. S.; Shih, W. C. Magnetic Active Water Filter Membrane for Induced Heating to Remove Biofoulants. *ACS Appl. Mater. Interfaces* **2020**, *12* (9), 10291−10298.

(3) Novickij, V.; Stanevičiene, R.; Vepštaite-Monstaviče, I.; Gruškiene, R.; Krivorotova, T.; Sereikaite, J.; Novickij, J.; Serviene, E. Overcoming Antimicrobial Resistance in Bacteria Using Bioactive Magnetic Nanoparticles and Pulsed Electromagnetic Fields. *Front. Microbiol.* **2018**, *8*, 2678.

(4) Pankhurst, Q. A.; Thanh, N. K. T.; Jones, S. K.; Dobson, J. Progress in Applications of Magnetic Nanoparticles in Biomedicine. *J. Phys. D: Appl. Phys.* **2009**, *42*, 224001.

(5) Wang, L.; Hervault, A.; Southern, P.; Sandre, O.; Couillaud, F.; Thanh, N. T. K. In Vitro Exploration of the Synergistic Effect of Alternating Magnetic Field Mediated Thermo-Chemotherapy with Doxorubicin Loaded Dual PH- And Thermo-Responsive Magnetic Nanocomposite Carriers. *J. Mater. Chem. B* **2020**, *8* (46), 10527−10539.

(6) Hachani, R.; Lowdell, M.; Birchall, M.; Hervault, A.; Mertz, D.; Begin-Colin, S.; Thanh, N. T. K. Polyol Synthesis, Functionalisation, and Biocompatibility Studies of Superparamagnetic Iron Oxide Nanoparticles as Potential MRI Contrast Agents. *Nanoscale* **2016**, *8* (6), 3278−3287.

(7) Bao, Y.; Sherwood, J. A.; Sun, Z. Magnetic Iron Oxide Nanoparticles as: T 1 Contrast Agents for Magnetic Resonance Imaging. *J. Mater. Chem. C* **2018**, *6* (6), 1280−1290.

(8) Gilchrist, R. K.; Medal, R.; Shorey, W. D.; Hanselman, R. C.; Parrott, J. C.; Taylor, C. B. Selective Inductive Heating of Lymph Nodes. *Ann. Surg.* **1957**, *146* (4), 596−606.

(9) Nguyen, V. T. A.; De Pauw-Gillet, M. C.; Gauthier, M.; Sandre, O. Magnetic Polyion Complex Micelles for Cell Toxicity Induced by Radiofrequency Magnetic Field Hyperthermia. *Nanomaterials* **2018**, *8*, 1014.

(10) Blanco-Andujar, C.; Ortega, D.; Southern, P.; Nesbitt, S. A.; Thanh, N. T. K.; Pankhurst, Q. A. Real-Time Tracking of Delayed-Onset Cellular Apoptosis Induced by Intracellular Magnetic Hyperthermia. *Nanomedicine* **2016**, *11* (2), 121−136.

(11) Alphandéry, E. Bio-Synthesized Iron Oxide Nanoparticles for Cancer Treatment. *Int. J. Pharm.* **2020**, *586* (March), 119472.

(12) Mandawala, C.; Chebbi, I.; Durand-Dubief, M.; Le Fèvre, R.; Hamdous, Y.; Guyot, F.; Alphandéry, E. Biocompatible and Stable Magnetosome Minerals Coated with Poly-l-Lysine, Citric Acid, Oleic Acid, and Carboxy-Methyl-Dextran for Application in the Magnetic Hyperthermia Treatment of Tumors. *J. Mater. Chem. B* **2017**, *5* (36), 7644−7660.

(13) Nguyen, T. K.; Duong, H. T. T.; Selvanayagam, R.; Boyer, C.; Barraud, N. Iron Oxide Nanoparticle-Mediated Hyperthermia Stimulates Dispersal in Bacterial Biofilms and Enhances Antibiotic Efficacy. *Sci. Rep.* **2015**, *5*, 18385.

(14) Biase, J. N.; Whitehead, E. D.; Miller, F.; Hoffman, S. Unilateral Unitary Inflatable Penile Prosthesis to Correct Impaired Tumescence and Severe Penile Deformity Resulting from Traumatic Rupture of 1 Corpus Cavernosum. *J. Urol.* **1994**, *152* (6), 2098−2100.

(15) Tong, S.; Quinto, C. A.; Zhang, L.; Mohindra, P.; Bao, G. Size-Dependent Heating of Magnetic Iron Oxide Nanoparticles. *ACS Nano* **2017**, *11* (7), 6808−6816.

(16) Lartigue, L.; Innocenti, C.; Kalaivani, T.; Awwad, A.; Sanchez Duque, M. d. M.; Guari, Y.; Larionova, J.; Guerin, C.; Montero, J.-L. G.; Barragan-Montero, V.; Arosio, P.; Lascialfari, A.; Gatteschi, D.; Sangregorio, C. Water-Dispersible Sugar-Coated Iron Oxide Nanoparticles. An Evaluation of Their Relaxometric and Magnetic Hyperthermia Properties. *J. Am. Chem. Soc.* **2011**, *133* (27), 10459−10472.

(17) Blanco-Andujar, C.; Ortega, D.; Southern, P.; Pankhurst, Q. A.; Thanh, N. T. K. High Performance Multi-Core Iron Oxide Nanoparticles for Magnetic Hyperthermia: Microwave Synthesis, and the Role of Core-to-Core Interactions. *Nanoscale* **2015**, *7* (5), 1768−1775.

(18) Hu, F.; MacRenaris, K. W.; Waters, E. A.; Schultz-Sikma, E. A.; Eckermann, A. L.; Meade, T. J. Highly Dispersible, Superparamagnetic Magnetite Nanoflowers for Magnetic Resonance Imaging. *Chem. Commun.* **2010**, *46* (1), 73−75.

(19) Besenhard, M. O.; LaGrow, A. P.; Hodzic, A.; Kriechbaum, M.; Panariello, L.; Bais, G.; Loizou, K.; Damilos, S.; Margarida Cruz, M.; Thi Kim Thanh, N.; Gavriilidis, A. Co-Precipitation Synthesis of Stable Iron Oxide Nanoparticles with NaOH: New Insights and Continuous Production via Flow Chemistry. *Chem. Eng. J.* **2020**, *399*, 125740.

(20) Blanco-Andujar, C.; Ortega, D.; Pankhurst, Q. A.; Thanh, N. T. K. Elucidating the Morphological and Structural Evolution of Iron Oxide Nanoparticles Formed by Sodium Carbonate in Aqueous Medium. *J. Mater. Chem.* **2012**, *22* (25), 12498−12506.

(21) Besenhard, M. O.; Panariello, L.; Kiefer, C.; LaGrow, A. P.; Storozhuk, L.; Perton, F.; Begin, S.; Mertz, D.; Thanh, N. T. K.; Gavriilidis, A. Small Iron Oxide Nanoparticles as MRI T 1 Contrast Agent: Scalable Inexpensive Water-Based Synthesis Using a Flow Reactor. *Nanoscale* **2021**, *13*, 8795.

(22) Besenhard, M. O.; Lagrow, A. P.; Famiani, S.; Pucciarelli, M.; Lettieri, P.; Thanh, N. T. K.; Gavriilidis, A. Continuous Production of Iron Oxide Nanoparticles: Via Fast and Economical High Temperature Synthesis. *React. Chem. Eng.* **2020**, *5* (8), 1474−1483.
(23) Laurent, S.; Forge, D.; Port, M.; Roch, A.; Robic, C.; Vander Elst, L.; Muller, R. N. Magnetic Iron Oxide Nanoparticles: Synthesis, Stabilization, Vectorization, Physicochemical Characterizations, and Biological Applications. *Chem. Rev.* **2008**, *108* (6), 2064−2110.
(24) Wegmann, M.; Scharr, M. *Synthesis of Magnetic Iron Oxide Nanoparticles*; Elsevier Inc.: Amsterdam, 2018 DOI: 10.1016/B978-0-12-805364-5.00008-1.
(25) Kotoulas, A.; Dendrinou-Samara, C.; Angelakeris, M.; Kalogirou, O. The Effect of Polyol Composition on the Structural and Magnetic Properties of Magnetite Nanoparticles for Magnetic Particle Hyperthermia. *Materials* **2019**, *12*, 2663.
(26) Majidi, S.; Zeinali Sehrig, F.; Farkhani, S. M.; Soleymani Goloujeh, M.; Akbarzadeh, A. Current Methods for Synthesis of Magnetic Nanoparticles. *Artif. Cells, Nanomed., Biotechnol.* **2016**, *44* (2), 722−734.
(27) Fievet, F.; Ammar-Merah, S.; Brayner, R.; Chau, F.; Giraud, M.; Mammeri, F.; Peron, J.; Piquemal, J. Y.; Sicard, L.; Viau, G. The Polyol Process: A Unique Method for Easy Access to Metal Nanoparticles with Tailored Sizes, Shapes and Compositions. *Chem. Soc. Rev.* **2018**, *47* (14), 5187−5233.
(28) Chakroune, N.; Viau, G.; Ammar, S.; Jouini, N.; Gredin, P.; Vaulay, M. J.; Fiévet, F. Synthesis, Characterization and Magnetic Properties of Disk-Shaped Particles of a Cobalt Alkoxide: CoII-(C2H4O 2). *New J. Chem.* **2005**, *29* (2), 355−361.
(29) Sanchez, L. M.; Martin, D. A.; Alvarez, V. A.; Gonzalez, J. S. Polyacrylic Acid-Coated Iron Oxide Magnetic Nanoparticles: The Polymer Molecular Weight Influence. *Colloids Surf., A* **2018**, *543*, 28−37.
(30) Mi, X.; Tong, M.; Cai, J.; Su, H.; Liu, S.; Ma, Y.; Wei, X.; Zhang, C. Facile Synthesis of Superparamagnetic Iron Oxide Nanoparticles with Tunable Size: From Individual Nanoparticles to Nanoclusters. *Micro Nano Lett.* **2017**, *12* (10), 749−753.
(31) Shahid, M. K.; Kim, Y.; Choi, Y. G. Adsorption of Phosphate on Magnetite-Enriched Particles (MEP) Separated from the Mill Scale. *Front. Environ. Sci. Eng.* **2019**, *13*, 71.
(32) Daou, T. J.; Begin-Colin, S.; Grenèche, J. M.; Thomas, F.; Derory, A.; Bernhardt, P.; Legaré, P.; Pourroy, G. Phosphate Adsorption Properties of Magnetite-Based Nanoparticles. *Chem. Mater.* **2007**, *19* (18), 4494−4505.
(33) Sahoo, Y.; Pizem, H.; Fried, T.; Golodnitsky, D.; Burstein, L.; Sukenik, C. N.; Markovich, G. Alkyl Phosphonate/Phosphate Coating on Magnetite Nanoparticles: A Comparison with Fatty Acids. *Langmuir* **2001**, *17* (25), 7907−7911.
(34) Majeed, J.; Barick, K. C.; Shetake, N. G.; Pandey, B. N.; Hassan, P. A.; Tyagi, A. K. Water-Dispersible Polyphosphate-Grafted Fe3O4 Nanomagnets for Cancer Therapy. *RSC Adv.* **2015**, *5* (105), 86754−86762.
(35) Rubia-Rodríguez, I.; Santana-Otero, A.; Spassov, S.; Tombácz, E.; Johansson, C.; De La Presa, P.; Teran, F. J.; Morales, M. D. P.; Veintemillas-Verdaguer, S.; Thanh, N. T. K.; Besenhard, M. O.; Wilhelm, C.; Gazeau, F.; Harmer, Q.; Mayes, E.; Manshian, B. B.; Soenen, S. J.; Gu, Y.; Millán, Á.; Efthimiadou, E. K.; Gaudet, J.; Goodwill, P.; Mansfield, J.; Steinhoff, U.; Wells, J.; Wiekhorst, F.; Ortega, D. Whither Magnetic Hyperthermia? A Tentative Roadmap. *Materials* **2021**, *14*, 706.
(36) Gavilán, H.; Sánchez, E. H.; Brollo, M. E. F.; Asín, L.; Moerner, K. K.; Frandsen, C.; Lázaro, F. J.; Serna, C. J.; Veintemillas-Verdaguer, S.; Morales, M. P.; Gutiérrez, L. Formation Mechanism of Maghemite Nanoflowers Synthesized by a Polyol-Mediated Process. *ACS Omega* **2017**, *2* (10), 7172−7184.
(37) Ramesh, R.; Rajalakshmi, M.; Muthamizhchelvan, C.; Ponnusamy, S. Synthesis of Fe3O4 Nanoflowers by One Pot Surfactant Assisted Hydrothermal Method and Its Properties. *Mater. Lett.* **2012**, *70*, 73−75.
(38) Wang, L.; Gao, L. Morphology Transformation of Hematite Nanoparticles through Oriented Aggregation. *J. Am. Ceram. Soc.* **2008**, *91* (10), 3391−3395.
(39) Zhang, B.; Tu, Z.; Zhao, F.; Wang, J. Superparamagnetic Iron Oxide Nanoparticles Prepared by Using an Improved Polyol Method. *Appl. Surf. Sci.* **2013**, *266*, 375−379.
(40) Thanh, N. T. K.; Maclean, N.; Mahiddine, S. Mechanisms of Nucleation and Growth of Nanoparticles in Solution. *Chem. Rev.* **2014**, *114* (15), 7610−7630.
(41) Cai, W.; Wan, J. Facile Synthesis of Superparamagnetic Magnetite Nanoparticles in Liquid Polyols. *J. Colloid Interface Sci.* **2007**, *305* (2), 366−370.
(42) Rui, Y. P.; Liang, B.; Hu, F.; Xu, J.; Peng, Y. F.; Yin, P. H.; Duan, Y.; Zhang, C.; Gu, H. Ultra-Large-Scale Production of Ultrasmall Superparamagnetic Iron Oxide Nanoparticles for T1-Weighted MRI. *RSC Adv.* **2016**, *6* (27), 22575−22585.
(43) Hemery, G.; Keyes, A. C.; Garaio, E.; Rodrigo, I.; Garcia, J. A.; Plazaola, F.; Garanger, E.; Sandre, O. Tuning Sizes, Morphologies, and Magnetic Properties of Monocore Versus Multicore Iron Oxide Nanoparticles through the Controlled Addition of Water in the Polyol Synthesis. *Inorg. Chem.* **2017**, *56* (14), 8232−8243.
(44) Palchoudhury, S.; Xu, Y.; Rushdi, A.; Holler, R. A.; Bao, Y. Controlled Synthesis of Iron Oxide Nanoplates and Nanoflowers. *Chem. Commun.* **2012**, *48* (85), 10499−10501.
(45) Cabana, S.; Curcio, A.; Michel, A.; Wilhelm, C.; Abou-Hassan, A. Iron Oxide Mediated Photothermal Therapy in the Second Biological Window: A Comparative Study between Magnetite/Maghemite Nanospheres and Nanoflowers. *Nanomaterials* **2020**, *10*, 1548.
(46) Hemery, G.; Genevois, C.; Couillaud, F.; Lacomme, S.; Gontier, E.; Ibarboure, E.; Lecommandoux, S.; Garanger, E.; Sandre, O. Monocore: Vs. Multicore Magnetic Iron Oxide Nanoparticles: Uptake by Glioblastoma Cells and Efficiency for Magnetic Hyperthermia. *Mol. Syst. Des. Eng.* **2017**, *2* (5), 629−639.
(47) Javed, Y.; Lartigue, L.; Hugounenq, P.; Vuong, Q. L.; Gossuin, Y.; Bazzi, R.; Wilhelm, C.; Ricolleau, C.; Gazeau, F.; Alloyeau, D. Biodegradation Mechanisms of Iron Oxide Monocrystalline Nanoflowers and Tunable Shield Effect of Gold Coating. *Small* **2014**, *10* (16), 3325−3337.
(48) Hugounenq, P.; Levy, M.; Alloyeau, D.; Lartigue, L.; Dubois, E.; Cabuil, V.; Ricolleau, C.; Roux, S.; Wilhelm, C.; Gazeau, F.; Bazzi, R. Iron Oxide Monocrystalline Nanoflowers for Highly Efficient Magnetic Hyperthermia. *J. Phys. Chem. C* **2012**, *116* (29), 15702−15712.
(49) Lartigue, L.; Hugounenq, P.; Alloyeau, D.; Clarke, S. P.; Lévy, M.; Bacri, J. C.; Bazzi, R.; Brougham, D. F.; Wilhelm, C.; Gazeau, F. Cooperative Organization in Iron Oxide Multi-Core Nanoparticles Potentiates Their Efficiency as Heating Mediators and MRI Contrast Agents. *ACS Nano* **2012**, *6* (12), 10935−10949.
(50) Abutalib, N. H.; Lagrow, A. P.; Besenhard, M. O.; Bondarchuk, O.; Sergides, A.; Famiani, S.; Ferreira, L. P.; Cruz, M. M.; Gavriilidis, A.; Thanh, N. T. K. Shape Controlled Iron Oxide Nanoparticles: Inducing Branching and Controlling Particle Crystallinity. *CrystEngComm* **2021**, *23* (3), 550−561.
(51) De La Presa, P.; Luengo, Y.; Multigner, M.; Costo, R.; Morales, M. P.; Rivero, G.; Hernando, A. Study of Heating Efficiency as a Function of Concentration, Size, and Applied Field in γ-Fe2O3 Nanoparticles. *J. Phys. Chem. C* **2012**, *116* (48), 25602−25610.
(52) Sakellari, D.; Brintakis, K.; Kostopoulou, A.; Myrovali, E.; Simeonidis, K.; Lappas, A.; Angelakeris, M. Ferrimagnetic Nanocrystal Assemblies as Versatile Magnetic Particle Hyperthermia Mediators. *Mater. Sci. Eng., C* **2016**, *58*, 187−193.
(53) Shaw, S. K.; Biswas, A.; Gangwar, A.; Maiti, P.; Prajapat, C. L.; Meena, S. S.; Prasad, N. K. Synthesis of Exchange Coupled Nanoflowers for Efficient Magnetic Hyperthermia. *J. Magn. Magn. Mater.* **2019**, *484*, 437−444.
(54) Xu, W.; Wang, S.; Li, A.; Wang, X. Synthesis of Aminopropyltriethoxysilane Grafted/Tripolyphosphate Intercalated ZnAl LDHs and Their Performance in the Flame Retardancy and Smoke

Suppression of Polyurethane Elastomer. *RSC Adv.* **2016**, *6* (53), 48189−48198.
(55) Bañobre-López, M.; Teijeiro, A.; Rivas, J. Magnetic Nanoparticle-Based Hyperthermia for Cancer Treatment. *Reports Pract. Oncol. Radiother.* **2013**, *18* (6), 397−400.
(56) Lappas, A.; Antonaropoulos, G.; Brintakis, K.; Vasilakaki, M.; Trohidou, K. N.; Iannotti, V.; Ausanio, G.; Kostopoulou, A.; Abeykoon, M.; Robinson, I. K.; Bozin, E. S. Vacancy-Driven Noncubic Local Structure and Magnetic Anisotropy Tailoring in FexO-Fe3-δ O4 Nanocrystals. *Phys. Rev. X* **2019**, *9* (4), 41044.
(57) Kallumadil, M.; Tada, M.; Nakagawa, T.; Abe, M.; Southern, P.; Pankhurst, Q. A. Suitability of Commercial Colloids for Magnetic Hyperthermia. *J. Magn. Magn. Mater.* **2009**, *321* (10), 1509−1513.
(58) Sakellari, D.; Mathioudaki, S.; Kalpaxidou, Z.; Simeonidis, K.; Angelakeris, M. Exploring Multifunctional Potential of Commercial Ferrofluids by Magnetic Particle Hyperthermia. *J. Magn. Magn. Mater.* **2015**, *380*, 360−364.
(59) Niculaes, D.; Lak, A.; Anyfantis, G. C.; Marras, S.; Laslett, O.; Avugadda, S. K.; Cassani, M.; Serantes, D.; Hovorka, O.; Chantrell, R.; Pellegrino, T. Asymmetric Assembling of Iron Oxide Nanocubes for Improving Magnetic Hyperthermia Performance. *ACS Nano* **2017**, *11* (12), 12121−12133.
(60) Lak, A.; Cassani, M.; Mai, B. T.; Winckelmans, N.; Cabrera, D.; Sadrollahi, E.; Marras, S.; Remmer, H.; Fiorito, S.; Cremades-Jimeno, L.; Litterst, F. J.; Ludwig, F.; Manna, L.; Teran, F. J.; Bals, S.; Pellegrino, T. Fe2+ Deficiencies, FeO Subdomains, and Structural Defects Favor Magnetic Hyperthermia Performance of Iron Oxide Nanocubes into Intracellular Environment. *Nano Lett.* **2018**, *18* (11), 6856−6866.
(61) Orozco-Henao, J. M.; Muraca, D.; Sánchez, F. H.; Mendoza Zélis, P. Palmitic Acid-Coated Magnetite Nanocubes with High-Quality Crystallinity and Bulk-like Magnetic Features. *J. Phys. D: Appl. Phys.* **2020**, *53*, 385001.
(62) Atkinson, W. J.; Brezovich, I. A.; Chakraborty, D. P. Usable Frequencies in Hyperthermia with Thermal Seeds. *IEEE Trans. Biomed. Eng.* **1984**, *BME-31* (1), 70−75.
(63) Thiesen, B.; Jordan, A. Clinical Applications of Magnetic Nanoparticles for Hyperthermia. *Int. J. Hyperthermia* **2008**, *24* (6), 467−474.
(64) Kossatz, S.; Ludwig, R.; Dähring, H.; Ettelt, V.; Rimkus, G.; Marciello, M.; Salas, G.; Patel, V.; Teran, F. J.; Hilger, I. High Therapeutic Efficiency of Magnetic Hyperthermia in Xenograft Models Achieved with Moderate Temperature Dosages in the Tumor Area. *Pharm. Res.* **2014**, *31* (12), 3274−3288.
(65) Mamiya, H. Recent Advances in Understanding Magnetic Nanoparticles in Ac Magnetic Fields and Optimal Design for Targeted Hyperthermia. *J. Nanomater.* **2013**, *2013*, 752973.
(66) Simeonidis, K.; Morales, M. P.; Marciello, M.; Angelakeris, M.; De La Presa, P.; Lazaro-Carrillo, A.; Tabero, A.; Villanueva, A.; Chubykalo-Fesenko, O.; Serantes, D. In-Situ Particles Reorientation during Magnetic Hyperthermia Application: Shape Matters Twice. *Sci. Rep.* **2016**, *6*, 38382.
(67) Natividad, E.; Castro, M.; Mediano, A. Adiabatic vs. Non-Adiabatic Determination of Specific Absorption Rate of Ferrofluids. *J. Magn. Magn. Mater.* **2009**, *321* (10), 1497−1500.
(68) Wan, J.; Cai, W.; Meng, X.; Liu, E. Monodisperse Water-Soluble Magnetite Nanoparticles Prepared by Polyol Process for High-Performance Magnetic Resonance Imaging. *Chem. Commun.* **2007**, 5004−5006.
(69) Wan, J.; Yuan, R.; Zhang, C.; Wu, N.; Yan, F.; Yu, S.; Chen, K. Stable and Biocompatible Colloidal Dispersions of Superparamagnetic Iron Oxide Nanoparticles with Minimum Aggregation for Biomedical Applications. *J. Phys. Chem. C* **2016**, *120* (41), 23799−23806.
(70) Wildeboer, R. R.; Southern, P.; Pankhurst, Q. A. On the Reliable Measurement of Specific Absorption Rates and Intrinsic Loss Parameters in Magnetic Hyperthermia Materials. *J. Phys. D: Appl. Phys.* **2014**, *47* (49), 495003.

https://doi.org/10.1021/acsami.1c12323
ACS Appl. Mater. Interfaces 2021, 13, 45870−45880